Journal of Natural Gas Science and Engineering 18 (2014) 406–411

Contents lists available at ScienceDirect

Journal of Natural Gas Science and Engineering

journal homepage: www.elsevier.com/locate/jngse

Oxidative coupling of methane with La_2O_3–CeO_2 nanofiber fabrics: A reaction engineering study

Daniel Noon, Bahman Zohour, Selim Senkan*

Department of Chemical Engineering, University of California, Los Angeles, CA 90095, USA

ARTICLE INFO

Article history:
Received 29 January 2014
Received in revised form
6 April 2014
Accepted 7 April 2014
Available online 23 April 2014

Keywords:
OCM
Natural gas processing
Nanofiber catalyst
Electrospinning
Exothermic reactions
Rare earth oxide catalysts

ABSTRACT

The effects of changes in various operating conditions were explored on the performance of an oxidative coupling of methane (OCM) reaction using La_2O_3–CeO_2 nanofiber fabric catalysts in a packed bed reactor. The operating conditions were: 1 atm pressure, CH_4/O_2 ratio 4–7, feed flow rate 80–320 sccm, catalyst loading 5–20 mg, feed gas temperature 300–620 °C. These studies revealed that the rates of the OCM reaction is largely dominated by mass transfer limitations as evidenced by increases in reactor bed temperatures with increasing feed flow rates. C_{2+} selectivities and yields of up to 70% and 18% respectively were also attained. Experiments with different catalyst loadings indicated that short catalytic beds are preferred for increasing C_{2+} selectivities in OCM reactors.

© 2014 Elsevier B.V. All rights reserved.

1. Introduction

The direct utilization of methane, the main component of natural gas (NG), as an alternate chemical feedstock to petroleum, has been a highly desirable but difficult goal in industrial catalysis (Alvarez-Galvan et al., 2011). Many direct and indirect methods have been studied for CH_4 conversion into more useful products, including olefins (e.g. C_2H_4, C_3H_6), higher molecular weight hydrocarbons and liquids (e.g. benzene and gasoline), as discussed in a recent review (Alvarez-Galvan et al., 2011). The production of ethylene from NG represents a particularly significant opportunity because of its massive worldwide use as an intermediate in the production of plastics, such as polyethylene and polyvinyl chloride. In addition, ethylene can be oligomerized into liquid hydrocarbons, such as alpha olefins, thereby enabling the efficient utilization of NG in remote parts of the world. At present, ethylene is primarily produced by the steam cracking of naphtha, a petroleum product. All indirect NG conversion routes utilize the high temperature, endothermic and costly steam reforming as a first step, where synthesis gas (H_2/CO mixtures) is produced. This is followed by the synthesis of useful products via various catalytic processes (Alvarez-Galvan et al., 2011). Although direct methods avoid use of costly syngas steps, they remain uneconomical due in part to low C_{2+} yields, high temperatures and low throughputs. High temperatures are particularly detrimental since they result in catalyst deactivation and create materials problems for reactors.

In the oxidative coupling of methane (OCM), CH_4 is directly converted to C_2H_6, C_2H_4 and H_2O in the presence of O_2 and a suitable catalyst (Alvarez-Galvan et al., 2011). The first step involves the abstraction of H from CH_4 by the catalyst to form methyl radicals (CH_3•) (Zavyalova et al., 2011; Lunsford, 1995). The coupling of two CH_3• then creates C_2H_6, followed by its dehydrogenation to C_2H_4. Some C_3 hydrocarbons also form by addition of CH_3• to C_2H_4 (Conway et al., 1991). However, undesirable surface and gas phase combustion reactions also lead to CO and CO_2 (CO_x). Since high temperatures promote homogeneous gas phase free radical reactions detrimental for C_{2+} products, the development of new catalysts that can operate at low temperatures is crucial for the economic viability of OCM. We recently reported promising results in OCM using catalytic nanofiber fabrics of La_2O_3–CeO_2 (Noon et al., 2013). This material was found to be advantageous over analogous powders previously reported in the literature (Dedov et al., 2003, 2005; Makhlin et al., 2009), especially in terms of the feed gas temperature required to activate methane (Noon et al., 2013). The CeO_2 is well recognized to promote La_2O_3 with regard to the OCM reaction (Dedov et al., 2003, 2005; Makhlin et al., 2009).

There are two prevailing OCM mechanisms in relation to La_2O_3 surfaces: the idea that a lattice oxygen is responsible for activation

* Corresponding author. Tel.: +1 310 206 4106; fax: +1 310 206 4107.
E-mail address: ssenkan@gmail.com (S. Senkan).

http://dx.doi.org/10.1016/j.jngse.2014.04.004
1875-5100/© 2014 Elsevier B.V. All rights reserved.

of the C–H bond on CH_4 either through a Mars–van Krevelen mechanism or through the dissociative adsorption of CH_4, where the fragments CH_3 and H bind to the surface oxide (Mleczko and Baerns, 1995; Li and Metiu, 2012; Hu et al., 2011); the dissociative adsorption of O_2 first onto the catalyst's oxide covered surface, forming a peroxy-type species that is responsible for subsequently activating the C–H bond (Palmer et al., 2002a, 2002b). Most of the remaining reactions occur in the gas phase, though it is suggested that CO_2 can be created by oxidation of an adsorbed methyl group in addition to through multiple gas phase routes. The difficulty in OCM is in isolating the products C_2H_4 and C_2H_6, which are susceptible to further oxidation, ultimately to CO_x.

The critical overall steps accepted to occur in the OCM mechanism, leading up to the formation of C_2H_6, are summarized in Eqs. (1)–(4):

$$O_2 + 2[*] \rightarrow 2[O] \quad (1)$$

$$CH_4 + [O] \rightarrow CH_3 + [OH] \quad (2)$$

$$CH_3 + CH_3 \rightarrow C_2H_6 \rightarrow C_2H_4 \rightarrow CO_x \quad (3)$$

$$[OH] + [OH] \rightarrow [O] + [*] + H_2O \quad (4)$$

where [*] is a vacant catalytic surface site. The direct oxidation of CH_4 to CO_2 as well as the oxidative dehydrogenation of C_2H_6 to C_2H_4 are also well accepted pathways in the OCM process. Additionally, there may be surface occupation by CO_2 as in Eq. (5):

$$CO_2 + [*] \rightarrow [CO_2] \quad (5)$$

which may block active sites from participating in OCM (Arndt et al., 2011; Xu et al., 1992; Istadi and Amin, 2006; Papa et al., 2011). The coupling of methyl radicals in Eq. (3) occurs in the gas phase while the formation of C_2H_4 and CO_x may either be catalytic or in the gas phase. The remaining reactions listed occur on the catalyst. In a highly exothermic catalytic reaction such as OCM, mass transfer limitations can be critical in determining reactor performance. This will be particularly important for the case of the limiting reactant O_2 in the current studies. At high temperatures, adsorption, surface reaction and desorption rates exceed mass diffusion rates (Mleczko and Baerns, 1995), rendering the latter as the rate determining process. Since mass transfer rates increase with increasing Reynolds number, the reactor bed temperatures would be expected to increase with increasing gas flow. However, the overall performance of the OCM reactors will be determined as a result of the competition between increased rates of reaction and shortened residence times with increased flow through the reactor.

Here, we report a follow-up study detailing some of the OCM reaction engineering aspects of the La_2O_3–CeO_2 catalyst developed in our laboratories. Reactor temperature profiles as well as reactor exit conversion and product selectivities are presented as a function of feed temperature, feed flow rate and composition.

2. Materials and methods

2.1. Electrospinning

Nanofibers are prepared by electrospinning (Tan et al., 2007). In a typical preparation, polyvinylpyrrolidone (PVP; 1.3 MDa) is mixed with a solvent containing water and ethanol (~1:2 weight ratio). To this solution, $La(NO_3)_3 \cdot 6H_2O$ and $Ce(NO_3)_3 \cdot 6H_2O$ are added. Water is necessary to allow for the mutual solubility of PVP and the metal salts while ethanol is used primarily to lower the surface tension of the solution, allowing it to be electrospun into fibers. The final solution is 6 wt% PVP with a metal-to-polymer weight ratio of 0.20.

The electrospinning setup in Fig. 1 features a syringe loaded with the spinning solution being pumped through a metal needle under 30 kV, causing streams to jet out towards the grounded collector, which has aluminum foil wrapped tightly around it. The syringe pump is programmed to then pump the fluid at a fixed rate of 1.0 mL/h. The material collected on the aluminum foil comprises nanofibers of PVP and the embedded La and Ce metal salts. After a sufficient amount of material is collected, the foil then is placed inside an oven for air calcination at 625 °C. This temperature allows for the fiber sample to be calcined without melting the foil. The La/Ce weight ratio of the material studied in this work is 3/1.

2.2. Catalytic performance testing

The nanofiber catalyst is packed in a 4 mm ID quartz tube, sandwiched between two quartz wool plugs and placed inside a temperature controlled tube furnace (Thermolyne® 21100). The reactor pressure is 1 atm. Inlet gas flow rates are regulated by electronic mass flow controllers (MKS, Burlington, MA). In this work, flow rates of 80–320 standard cubic centimeters per minute (sccm), catalyst weights of 5–20 mg (0.94 void fraction) and feed temperatures of 300–620 °C are examined. The inlet is a binary gas of CH_4 and O_2 with 75–87.5 mol% CH_4. Reaction products are sampled by a 300 micron ID capillary tubing and analyzed by on-line gas chromatography (Varian 4900 Micro-GC, with Molecular sieve X and Porapak U columns).

2.3. Temperature profiles

In separate experiments, a 0.25 mm diameter thermocouple (K-Type, Omega Engineering, CT) is placed inside the catalytic zone to measure the axial temperature profiles. The thermocouple is inserted tightly into a quartz capillary, the combination of which is placed on a micro-translation device that allows for precise incremental changes in the axial position of the thermocouple along the reactor (Zohour et al., 2013). In these experiments, 20 mg catalyst loading is used to form a bed depth of ~1.4 cm to improve the spatial resolution of the axial temperature profiles.

3. Results and discussion

3.1. Nanofibers

Shown in Fig. 2 is an SEM image of the calcined La_2O_3–CeO_2 nanofiber fabric. First and foremost, the fibers show considerable uniformity in diameter (~70 nm) and dispersion. BET area is about 25 m^2/g, suggesting the nanofibers are dense and do not possess internal porosity. Second, the fibers appear individually well

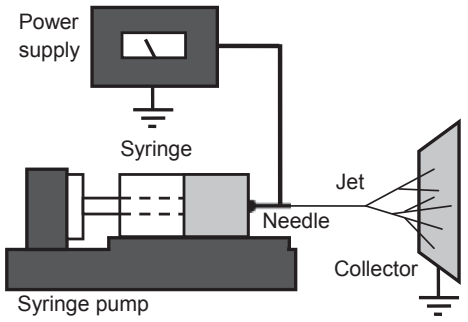

Fig. 1. Electrospinning setup used in the synthesis of La_2O_3–CeO_2 nanofibers.

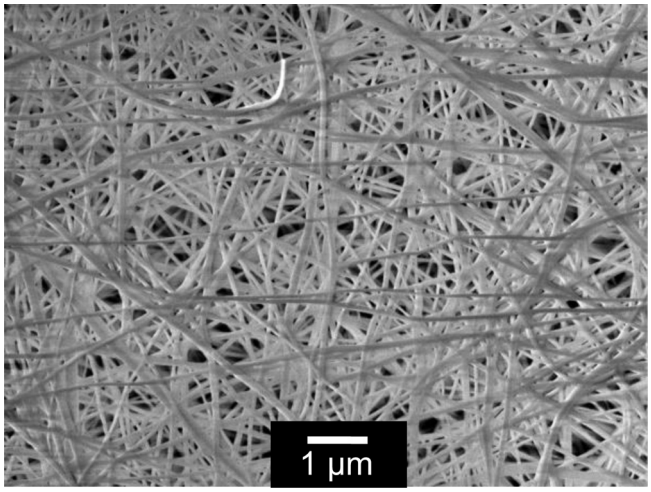

Fig. 2. SEM image of electrospun and subsequently calcined La_2O_3–CeO_2 fibers (diameter ~70 nm; magnification 13,000; working distance 6.7 mm; 4.0 kV).

exposed with little clustering, concomitant with the large and uniform interfiber space and a void fraction of 0.94. Although these features provide rapid access to and from active sites, which should be advantageous in improving the selectivity for labile products in partial oxidation reactions, they also promote homogeneous gas phase reactions. In contrast, co-precipitated La_2O_3–CeO_2 particles exhibit a high degree of agglomeration in which a significant fraction of La_2O_3–CeO_2 remain inaccessible or are accessible only through pores, concomitant with pore diffusion limitations and associated problems. Previously we demonstrated that La_2O_3–CeO_2 nanofiber fabric catalysts exhibit lower ignition temperatures and broader operating windows than the corresponding powder catalysts (Noon et al., 2013).

3.2. Feed temperature hysteresis

Before results are presented, it should be pointed out that the major C_2 products observed over La_2O_3–CeO_2 catalysts are C_2H_6 and C_2H_4, with the C_2H_6/C_2H_4 ratio being in the 1–2 range. In addition, some C_3H_6 is also formed constituting 5–8% of the C_{2+} products. Furthermore, some C_4 products were also consistently detected under OCM conditions, though in significantly lower amounts compared to the other products. The major undesirable products were CO_2 and CO.

In Fig. 3, the axial temperature profiles are presented for a CH_4/O_2 feed ratio of 5 and at a feed gas flow rate of $F = 160$ sccm with $m_{cat} = 20$ mg of catalyst packed into the bed at various feed gas temperatures T_f. Filled symbols represent the temperature profiles measured when the furnace temperature was stepwise heated up, while empty symbols were obtained during the stepwise cooling process. The temperature profile measurements were acquired while the reactant gases were flowing. The embedded thermocouple was used to monitor the establishment of the steady state bed temperature. Once the steady state temperature was reached (~30 min during heating and ~60 min during cooling), the temperature profile was measured by axially moving the thermocouple. After data acquisition, the furnace temperature was readjusted to its new set point. As seen in Fig. 3, the difference between the peak temperature in the catalytic zone and feed temperature T_f ranges between ~300 and 400 °C. This difference is at its largest at the lowest feed temperature $T_f = 390$ °C. However the locations of the peaks were noted to shift downstream during the cooling experiments, i.e. at values for T_f that are lower than the

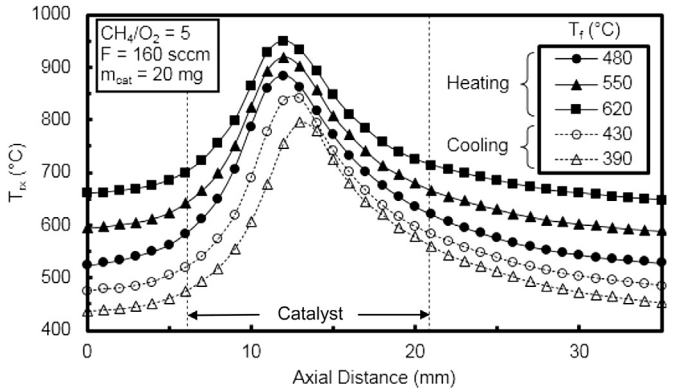

Fig. 3. Reactor temperature T_{rx} as a function of axial distance within and near the catalytic zone while increasing and decreasing the feed temperature T_f [480 (●), 550 (▲), 620 (■), 430 (○), 390 (Δ) °C] with the following fixed: CH_4/O_2 feed ratio of 5, catalyst weight of $m_{cat} = 20$ mg, flow rate of $F = 160$ sccm.

ignition temperature T_{ig}. This could also be due to insufficient cooling period (60 min) to attain steady state during the cooling process.

In Fig. 4, the accompanying reactor exit CH_4 conversions and C_{2+} selectivities are presented while Fig. 5 shows the O_2 conversions and C_2H_6/C_2H_4 ratios, both as a function of feed gas temperature T_f. As seen in Figs. 3 and 4, the onset of catalyst ignition was at 450 °C when *increasing* T_f, with a C_{2+} selectivity of 55% at 28% CH_4 conversion. Oxygen was completely consumed and the C_2H_6/C_2H_4 ratio was about 1 at the ignition point. For $T_f > T_{ig}$, the catalyst performance is limited by the exhaustion of O_2, with no change in the location of the peak bed temperature. As evident from Figs. 3 and 4, a hysteresis window was noted. On the *decreasing* T_f path, the high C_{2+} selectivity of 52–59% extended down to about 300 °C. Both the CH_4 and O_2 conversions steadily decreased and the C_2H_6/C_2H_4 ratio increased with decreasing T_f below the ignition temperature. These results are consistent with the lower catalyst peak temperature with decreasing T_f (Fig. 3).

3.3. Effect of feed flow rate and CH_4/O_2 ratio

In Fig. 6, the effects of feed gas flow rate on the spatial temperature profiles are presented at a CH_4/O_2 ratio of 5 and feed gas temperature of 570 °C. As evident from this figure, increasing feed gas flow rate dramatically increases the reactor temperature, while

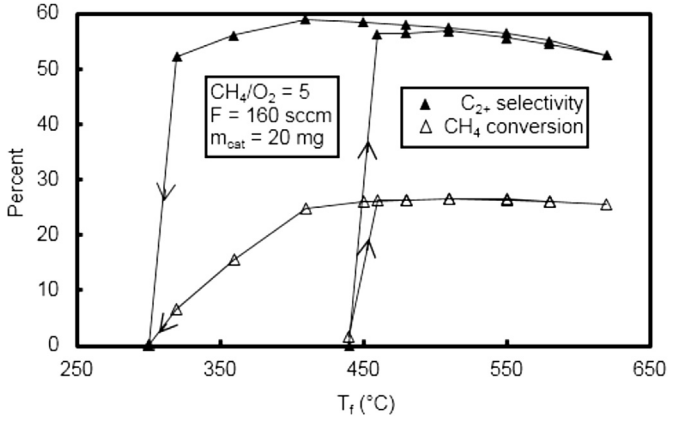

Fig. 4. C_{2+} selectivity (▲) and CH_4 conversion (Δ) as a function of feed temperature T_f, where the arrows indicate the increasing or decreasing path for T_f, with: CH_4/O_2 feed ratio of 5, catalyst weight of $m_{cat} = 20$ mg, flow rate of $F = 160$ sccm.

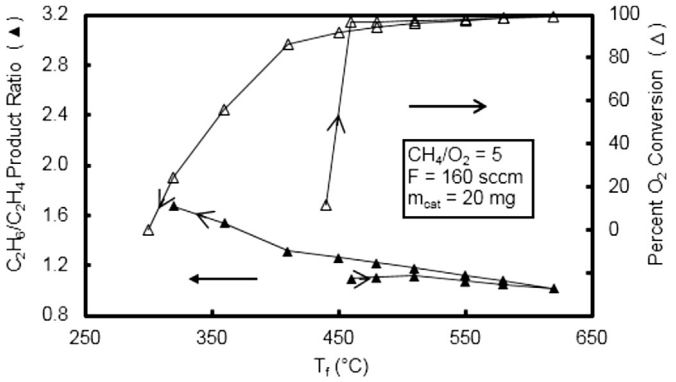

Fig. 5. Ethane-to-ethylene product ratio (left ordinate, ▲) and percent O_2 conversion (right ordinate, Δ) as a function of feed temperature T_f, where the arrows indicate the increasing or decreasing path for T_f, with: CH_4/O_2 feed ratio of 5, catalyst weight of $m_{cat} = 20$ mg, flow rate of $F = 160$ sccm.

only slightly shifting the location of the maximum temperature. For example, at 80 sccm flow, the peak temperature is 825 °C at ~12 mm within the bed. In contrast, at 200 sccm, the peak temperature reached 960 °C at ~11 mm. These results indicate that the rate of the OCM process in the experiments was significantly under the mass transfer limited conditions (Dalle Nogare et al., 2011). That is, the increased flow rates increased mass transfer coefficients and thus transport rates to the catalyst surface, thereby increasing the rates of the OCM reaction and thus heat generation rates. Increases in temperature results in the establishment of steeper temperature gradients which then lead to increased heat conduction both to upstream and downstream of the hot spot. On the other hand, increases in gas flow rates would decrease the residence times as well as convectively pushing the hot gases downstream. As a consequence of the complex combination of these conduction, convection and reaction processes, the peak temperatures can shift either upstream or downstream. Clearly, performing a detailed modeling work involving both the chemical kinetics and transport phenomena of the OCM process is called for.

Another possible contributor to the observed shifts in peak temperature locations in the OCM reactors is heat conduction in along thermocouple wires placed into the bed. Due to their higher thermal conductivity, metal thermocouples can transfer heat more efficiently than gases and the solid catalysts. As a result, thermocouples only provide spatially averaged readings, averaged along few bead or fiber diameters, especially when steep temperature gradients are present. Ideally, thermocouples should be placed perpendicular to gas flow, in order to accurately determine axial temperature profiles. However, such an option is not readily available for most catalytic reactor studies, including this work. In our experiments thermocouples were placed from the downstream side of the reactor.

In Fig. 7 the effect of CH_4/O_2 ratio on reactor temperature is shown. As can be seen, decreasing the CH_4/O_2 ratio from 7 to 4 increases the peak reactor temperature from 850 °C to 980 °C, while also resulting in a shift of the peak location from 12 mm to 10.8 mm. The increase in reactor bed temperature is the expected consequence of decreased methane dilution in the feed gas based on the overall OCM as well as combustion reaction stoichiometries.

In Figs. 8 and 9, CH_4 and O_2 conversions, C_{2+} selectivities and C_2H_6/C_2H_4 ratios are presented as a function of feed gas flow rate and CH_4/O_2 ratio at a feed gas temperature of $T_f = 570$ °C. An inspection of Fig. 8 reveals several interesting trends. First, increasing gas flow rates and decreasing CH_4/O_2 ratios have an adverse effect on C_{2+} selectivity, which reaches as high as 70% at a CH_4/O_2 feed ratio of 7 and feed flow rate of $F = 160$ sccm. The only exception to this trend is seen at the CH_4/O_2 ratio of 7 at low gas flow rates, which can be attributed to greater mass transfer limitations. Additionally, the depth of the catalyst bed could be a significant factor in creating low C_{2+} selectivities for low flow rates for the high CH_4/O_2 ratio. In a previous work when using an 8 mg La_2O_3–CeO_2 bed, a T_f hysteresis plot similar to that of Fig. 4 here was constructed (Noon et al., 2013). It was found that for a CH_4/O_2 feed ratio of 4 that C_{2+} selectivities reached their highest at the quench temperature of $T_f = 230$ °C. In Fig. 4 at the quench temperature, the C_{2+} selectivity is at one of its lowest observed values. A key difference between these two experiments is the bed depth, which clearly explains why C_{2+} selectivities are sacrificed at very low flow rates at $CH_4/O_2 = 7$. Over our OCM catalyst, we have previously shown that O_2 was completely consumed at about one-third of the 20 mg La_2O_3–CeO_2 bed (Zohour et al., 2013). This would not necessarily occur within a shallow 5 mg bed. That is, products of OCM with a deep bed are being exposed to the catalyst *at low temperatures*, that could lead to the destruction of C_{2+} products.

Second, methane conversions consistently increase with decreasing CH_4/O_2 ratio as a consequence of increased bed temperature caused by decreased methane dilution, reaching as high as 33% at a CH_4/O_2 feed ratio of 4 and the lowest feed rate examined of $F = 80$ sccm. Third, the effect of gas flow rates on methane conversions is complex. Methane conversion decreases with increasing

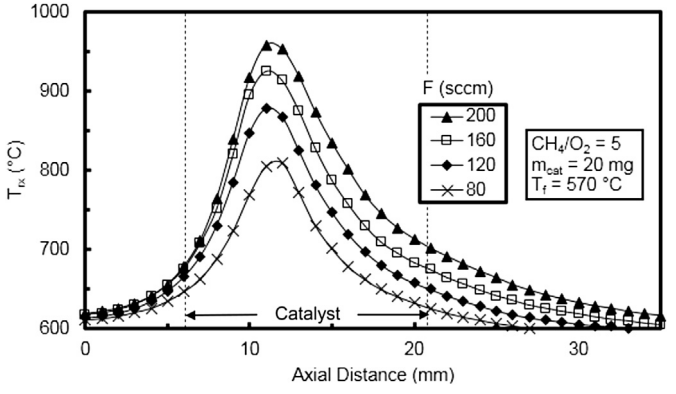

Fig. 6. Reactor temperature T_{rx} as a function of axial distance in the catalytic zone for various flow rates $F = 80$ (×), 120 (◆), 160 (□), 200 (▲) sccm, with the following fixed: CH_4/O_5 feed ratio of 5, catalyst weight of $m_{cat} = 20$ mg, feed temperature of $T_f = 570$ °C.

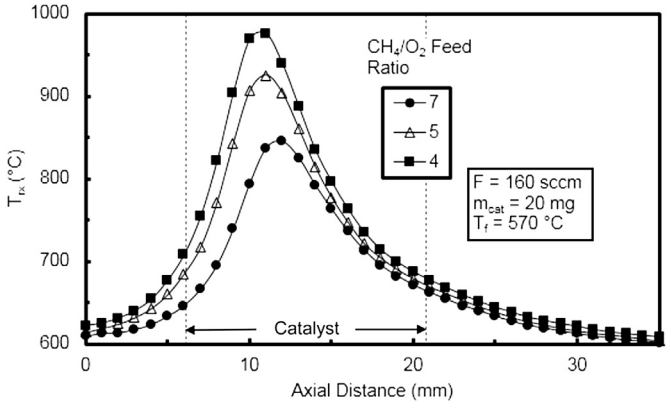

Fig. 7. Reactor temperature T_{rx} as a function of axial distance in the catalytic zone for the various feed CH_4/O_2 ratios of 4 (■), 5 (Δ), 7 (●), with the following fixed: feed flow rate of $F = 160$ sccm, catalyst weight of $m_{cat} = 20$ mg, feed temperature of $T_f = 570$ °C.

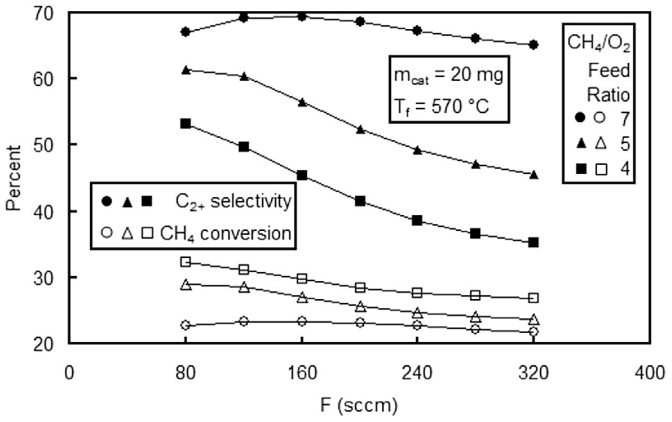

Fig. 8. C_{2+} selectivity (● ▲ ■) and CH_4 conversion (○ Δ □) as a function of flow rate and the CH_4/O_2 feed ratios of 4 (■ □), 5 (▲ Δ), 7 (● ○) with the following fixed: catalyst weight of m_{cat} = 20 mg, feed temperature of T_f = 570 °C.

gas flow rate for CH_4/O_2 ratios of 4 and 5, but the reverse trend is observed for 7. For the CH_4/O_2 ratios of 4 and 5 decreases in CH_4 conversions with increase in gas flow rate can readily be accounted for by the decreases in contact/reaction times since under these conditions the catalyst is at a sufficiently high temperature. Also, CO_x selectivities tend to be higher at larger flow rates due to higher temperatures. Since pathways that produce CO_x consume more O_2, less CH_4 will be converted at the end. From Fig. 9, the variation in oxygen conversion with respect to flow rate is less significant than for methane conversion, consistent with the argument that increasing CO_x selectivities with flow rates being the primary reason for the decreasing CH_4 conversions as opposed to reduced contact times. For the CH_4/O_2 ratio of 7 at 80 sccm, the catalyst temperature evidently is not hot enough resulting in increase in methane conversion slightly with increase in gas flow rate. This result is also in harmony with the results noted above.

Third, O_2 conversions uniformly increased with increasing gas flow and leveled off at higher flow rates for all CH_4/O_2 ratios (Fig. 9). Interestingly, O_2 conversions leveled off earlier and to a slightly lower level at the CH_4/O_2 ratio of 7. Fourth, C_2H_6/C_2H_4 ratios exhibited trends that consistently decreased with increasing gas flow rates and decreasing CH_4/O_2 ratios, an expected result based on increased reactor bed temperatures. The C_2H_6/C_2H_4 ratios were significantly higher (i.e. 1.3–1.6) at the CH_4/O_2 ratio of 7. For the CH_4/O_2 ratio of 4, the C_2H_6/C_2H_4 ratio decreased from 1.15 at 80 sccm to 0.95 at 320 sccm. Carbon dioxide, an abundant by-product in OCM, has also been documented as a catalyst poison and has strong binding affinity for highly basic materials (Papa et al., 2011). Consequently, under certain conditions CO_2 could limit the rates of the OCM reaction.

3.4. Effect of bed depth and space velocity

In order to better assess the importance of transport limitations relative to surface reactions, the performances of three reactors having 5, 10 and 20 mg catalyst loadings were investigated as a function of space velocity (i.e. F/m_{cat} = [Feed gas flow rate (sccm)]/[Catalyst weight (mg)]). In Figs. 10 and 11, CH_4 and O_2 conversions, and C_{2+} selectivities and C_2H_6/C_2H_4 ratios are presented respectively, as a function of space velocity for each of these packed beds. The CH_4/O_2 ratio was kept at 5 and the feed gas temperature was 570 °C in all of this set of experiments. An inspection of Fig. 10 reveals several trends. First, both the C_{2+} selectivities and methane conversions decreased with space velocity for all the three beds. Second, neither the methane conversion nor the C_{2+} selectivity profiles overlapped, clearly indicating that mass transfer rates were the limiting process in the OCM reaction. As seen in Fig. 10, C_{2+} selectivities were dramatically different, with the smaller packed bed reactor performing the best. For example, at the 15 sccm/mg space velocity, the C_{2+} selectivities were 64%, 55% and 45%, for the 5, 10 and 20 mg catalyst bed reactors, respectively. These results indicate that deeper bed reactors are detrimental in OCM as they result in the subsequent destruction of C_{2+} products once formed in the early part of the bed. Consequently, shallow bed reactors are desirable to maximize C_{2+} selectivities.

From Fig. 11, it can be seen that O_2 conversions in the shorter 5 mg bed were consistently lower at 85–93% than others both of which exhibited near complete oxygen consumption (>95%). Evidently, the 5 mg bed utilizes the reactants more efficiently towards OCM products while the other, i.e. deeper, beds lead to the subsequent combustion of C_{2+} products. These results are consistent with the higher C_{2+} selectivity of the 5 mg bed with its similar methane conversion (Fig. 10) and the lower C_{2+} selectivities of deeper beds.

The trends exhibited by the C_2H_6/C_2H_4 ratios were all similar, decreasing with increasing space velocity as a result of increasing reactor temperatures. However unlike C_{2+} selectivities, the deeper bed reactors were more beneficial for ethylene production. For

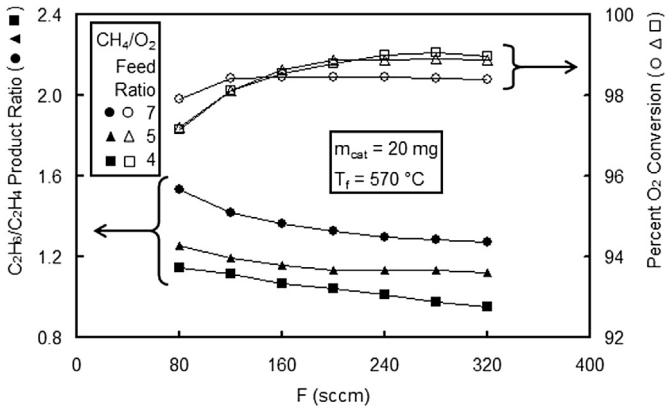

Fig. 9. Ethane-to-ethylene product ratio (left ordinate, ● ▲ ■) and percent O_2 conversion (right ordinate, ○ Δ □) as a function of feed flow rate and the CH_4/O_2 feed ratios of 4 (■ □), 5 (▲ Δ), 7 (● ○), with the following fixed: catalyst weight of m_{cat} = 20 mg, feed temperature of T_f = 570 °C.

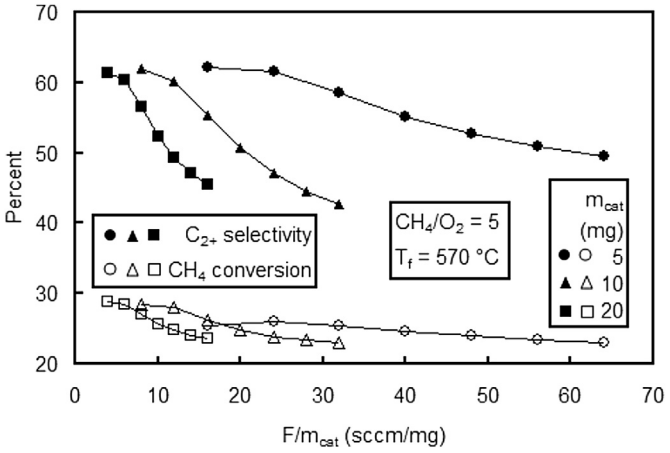

Fig. 10. C_{2+} selectivity (● ▲ ■) and CH_4 conversion (○ Δ □) as a function of space velocity F/m_{cat} and the catalyst weights of m_{cat} = 5 (● ○), 10 (▲ Δ), 20 (■ □) mg with the following fixed: CH_4/O_2 feed ratio of 5, feed temperature of T_f = 570 °C.

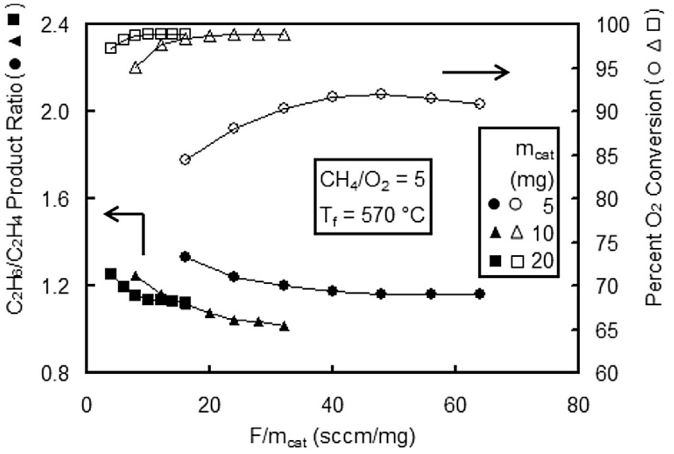

Fig. 11. Ethane-to-ethylene product ratio (left ordinate, ● ▲ ■) and percent O_2 conversion (right ordinate, ○ Δ □) as a function of space velocity F/m_{cat} and the catalyst weights of $m_{cat} = 5$ (● ○), 10 (▲ Δ), 20 (■ □) mg with the following fixed: CH_4/O_2 feed ratio of 5, feed temperature of $T_f = 570$ °C.

example, at space velocity of 20 sccm/mg, the C_2H_6/C_2H_4 ratios were 1.3 and 1.05 for the 5 mg and 10 mg beds, respectively. This appears to be due to increased rates of surface mediated ethane dehydrogenation through the deeper catalyst bed. If gas phase dehydrogenation processes were responsible, then the C_2H_6/C_2H_4 ratios would have been expected to be similar. These results are also consistent with a previous work in which concentration profiles in a similar reactor showed a delayed production of C_2H_4 relative to C_2H_6 (Zohour et al., 2013). Such a lag is expected since C_2H_4 is understood to be produced by the *sequential* catalytic dehydrogenation of C_2H_6.

3.5. Time on stream

In Fig. 12, the time on stream performance of the La_2O_3–CeO_2 nanofiber fabric catalyst is presented for over a 10 h continuous operation. The experimental conditions were: feed gas flow rate 80 sccm, 20 mg catalyst CH_4/O_2 ratio of 5, feed temperature 570 °C. As evident from Fig. 12, the La_2O_3–CeO_2 exhibits an excellent performance, showing no deterioration in activity and selectivity, rendering it a promising practical OCM catalyst.

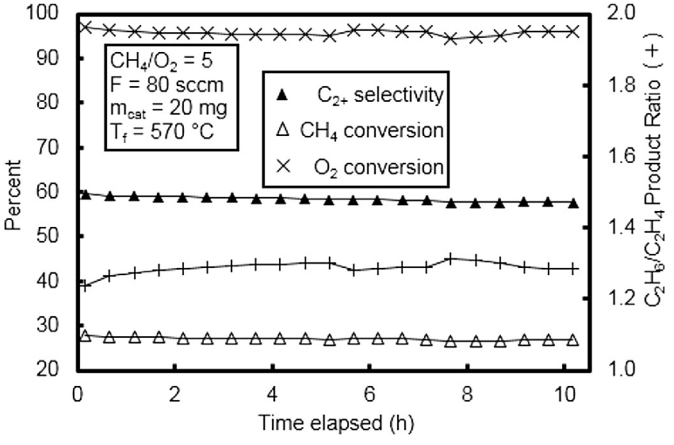

Fig. 12. Time on stream showing C_{2+} selectivity (▲), CH_4 conversion (Δ) and O_2 conversion (×) as a function of time with the following fixed: CH_4/O_2 feed ratio of 5, feed flow rate of $F = 80$ sccm, catalyst weight of $m_{cat} = 20$ mg, feed temperature of $T_f = 570$ °C.

4. Conclusions

In conclusion, the reaction engineering aspects of a La_2O_3–CeO_2 nanofiber fabric catalyst have been evaluated using packed bed reactors over a broad range of operating conditions. These studies indicated that the rates of the OCM reaction is largely dominated by mass transfer limitations, evidenced by the increases in the bed temperature with increasing feed flow rates. Our studies also revealed that short catalytic beds are preferred for increasing C_{2+} selectivities in OCM reactors. C_{2+} selectivities and yields of up to 70% and 18% respectively were also attained in this study.

Acknowledgments

We thank Laboratory Catalyst Systems (LCS) for use of its facilities and database. Daniel Noon acknowledges the NSF IGERT: Materials Creation Training Program (MCTP) – DGE-0654431 and the California NanoSystems Institute. Bahman Zohour acknowledges the University of California, Los Angeles (UCLA) Graduate Division Fellowship.

References

Alvarez-Galvan, M.C., Mota, N., Ojeda, M., Rojas, S., Navarro, R.M., Fierro, J.L.G., 2011. Direct methane conversion routes to chemicals and fuels. Catal. Today 171, 15.
Arndt, S., Laugel, G., Levchenko, S., Horn, R., Baerns, M., Scheffler, M., Schlogl, R., Schomacker, R., 2011. A critical assessment of Li/MgO-based catalysts for the oxidative coupling of methane. Catal. Rev. 53, 424.
Conway, S.J., Wang, D.J., Lunsford, J.H., 1991. Selective oxidation of methane and ethane over Li^+-MgO-Cl-catalysts promoted with metal oxides. Appl. Catal. A 79, L1.
Dalle Nogare, D., Degenstein, N.J., Horn, R., Canu, P., Schmidt, L.D., 2011. Modeling spatially resolved data of methane catalytic partial oxidation on Rh foam catalyst at different inlet compositions and flowrates. J. Catal. 277, 134.
Dedov, A.G., Loktev, A.S., Moiseev, I.I., Aboukais, A., Lamonier, J.-F., Filimonov, I.N., 2003. Oxidative coupling of methane catalyzed by rate earth oxides – unexpected synergistic effect of the oxide mixtures. Appl. Catal. A 245, 209.
Dedov, A.G., Moiseev, I.I., Loktev, A.S., Kuznetsov, N.T., Ketsko, V.A., Parkhomenko, K.V., Kartashev, I Yu, 2005. Catalytic synthesis of basic petrochemical products from $C_1 - C_4$ alkanes. Chem. Tech. Fuels Oils 41, 131.
Hu, Z., Li, B., Sun, X., Metiu, H., 2011. Chemistry of doped oxides: the activation of surface oxygen and the chemical compensation effect. J. Phys. Chem. C 115, 3065.
Istadi, Amin, N.A.S., 2006. Synergistic effect of catalyst basicity and reducibility on performance of ternary CeO_2-based catalyst for CO_2 OCM to C_2 hydrocarbons. J. Mol. Catal. A–Chem. 259, 61.
Li, B., Metiu, H., 2012. DFT studies of oxygen vacancies on undoped and doped La_2O_3 surfaces. J. Phys. Chem. C 114, 12234.
Lunsford, J.H., 1995. The catalytic oxidative coupling of methane. The catalytic oxidative coupling of methane. Angew. Chem. Int. Ed. 34, 970.
Makhlin, V.A., Podlesnaya, M.V., Dedov, A.G., Loktev, A.S., Tel'pukhovskaya, N.O., Moiseev, I.I., 2009. Oxidative dimerization of methane: kinetics, mathematical modeling, and optimization with La/Ce catalysts. Russ. J. Gen. Chem. 79, 2016.
Mleczko, L., Baerns, M., 1995. Catalytic oxidative coupling of methane – reaction engineering aspects and process schemes. Fuel Process. Technol. 42, 217.
Noon, D., Seubsai, A., Senkan, S., 2013. Oxidative coupling of methane by nanofiber catalysts. ChemCatChem 5, 146.
Palmer, M.S., Neurock, M., Olken, M.M., 2002a. Periodic density functional theory study of the dissociative adsorption of molecular oxygen over La_2O_3. J. Phys. Chem. B 106, 6543.
Palmer, M.S., Neurock, M., Olken, M.M., 2002b. Periodic density functional theory study of methane activation over La_2O_3: activity of O^{2-}, O^-, O_2^{2-}, oxygen point defect, and Sr^{2+}-doped surface sites. J. Am. Chem. Soc. 124, 8452.
Papa, F., Luminata, P., Osiceanu, P., Birjega, R., Akane, M., Balint, I., 2011. Acid-base properties of the active sites responsible for C_2^+ and CO_2 formation over MO-Sm_2O_3 (M = Zn, Mg, Ca and Sr) mixed oxides in OCM reaction. J. Mol. Catal. A–Chem. 346, 46.
Tan, S., Huang, X., Wu, B., 2007. Mini review – some fascinating phenomena in electrospinning processes and applications of electrospun nanofibers. Polym. Int. 56, 1330.
Xu, M.T., Shi, C.L., Yang, X.M., Rosynek, M.P., Lunsford, J.H., 1992. Effect of carbon dioxide on the activation energy for methyl radical generation over lithium/magnesia catalysts. J. Phys. Chem. 96, 6395.
Zavyalova, U., Holena, M., Schlogl, R., Baerns, M., 2011. Statistical analysis of past catalytic data on oxidative methane coupling for new insights into the composition of high-performance catalysts. ChemCatChem 3, 1935.
Zohour, B., Noon, D., Senkan, S., 2013. New insights into the oxidative coupling of methane from spatially resolved concentration and temperature profiles. ChemCatChem 5, 2809.